INTERNATIONAL JOURNAL OF
ENERGY RESEARCH

INTERNATIONAL JOURNAL OF ENERGY RESEARCH
Int. J. Energy Res. 2017; **41**:1277–1286
Published online 25 January 2017 in Wiley Online Library (wileyonlinelibrary.com). DOI: 10.1002/er.3710

Stability study of Bi-2212 conductor based on perturbation spectrum for hybrid superconducting magnet

Rui Kang[1], Jinxing Zheng[1,*,†], Yuntao Song[1,2], Lei Wang[1] and Xin He[1]

[1]University of Science and Technology of China, Hefei, China
[2]Institute of Plasma Physics, Chinese Academy of Science, Hefei, China

SUMMARY

A hybrid superconducting central solenoid employs Bi-2212 high-temperature superconductors and Nb3Sn low-temperature superconductors under the design of the Institute of Plasma Physics, Chinese Academy Of Science for further upgrade to CFETR, namely, the China Fusion Engineering Testing Reactor. The conductor type of both parts is cable-in-conduit conductors. This paper mainly focuses on stability study of the inner high-temperature superconductors part whose conductor works under a peak magnetic field of 16.79 T, and the maximum operating current of each turn is 50 kA. The simulation based on a 1-D simplified model is performed using the code THEA (thermal hydraulic and electric analysis of superconducting cable). Firstly, a brief analysis of stability considering the AC loss during current ramp-up is studied. Then, the stability margins in cases of different perturbations with varied lengths and durations are calculated, and a qualitative explanation of the result is proposed. Besides, the inlet pressure and pressure drop crucially influence the convection heat transfer between strands and helium; thus, the effect of these two factors on stability margin is discussed. All these results will provide important references for further optimization of this hybrid magnet. Copyright © 2017 John Wiley & Sons, Ltd.

KEY WORDS

nuclear energy; CFETR; HTS conductor; hybrid magnet; thermal stability; cable-in-conduit conductors

Correspondence
*Jinxing Zheng, Institute of Plasma Physics, Chinese Academy of Science, Hefei, China.
†E-mail: jxzheng@ipp.ac.cn

Received 5 June 2016; Revised 9 December 2016; Accepted 9 December 2016

1. INTRODUCTION

CFETR, which stands for China Fusion Engineering Testing Reactor, is a new fusion device designed by the China National Integration Design Group to fill the gap between international thermonuclear experimental reactor (ITER) and demonstration fusion reactor (DEMO), as shown in Figure 1 [1]. In the earlier concept design of CFETR, magnet system employs fully developed low-temperature superconductors (LTS) like Nb_3Sn and NbTi [2,3]. As for the further DEMO, however, higher magnetic field is needed to initiate, ramp up, sustain, and confine plasma in a larger device [4], which may be out of reach of the LTS materials because of their poor current carrying capacity under high magnetic field. In fact, even in CFETR, further upgrade may require higher magnetic field. Considering the significant progress of high-temperature superconductors (HTS), it is a good choice to replace LTS materials with them. Nevertheless, even the cheapest HTS material at present can cost two to five times than Nb_3Sn [5,6]. This economic issue, together with the relatively immature of fabrication technology of long length HTS wires or tapes, makes people become conservative on designing large magnet system with full HTS materials.

Therefore, in the Institute of Plasma Physics, Chinese Academy Of Science (ASIPP), a hybrid central solenoid magnet system consisting both LTS and HTS materials is designed. This hybrid magnet system prepared for upgrade of CFETR is divided into two parts, an outer LTS part and HTS insert coils. This kind of arrangement is a compromise between performance and economy. Compared with former full LTS scheme, the hybrid system, making use of good performance of HTS at high field, can reach higher volt seconds and maintain relatively compact while still being more economical than a full HTS one. Indeed, a similar design for toroidal field magnet system has already been proposed [7].

An overview of the geometry of the hybrid magnet and the LTS and HTS windings are shown in Figure 2. The outer LTS part uses Nb_3Sn superconductor as the original

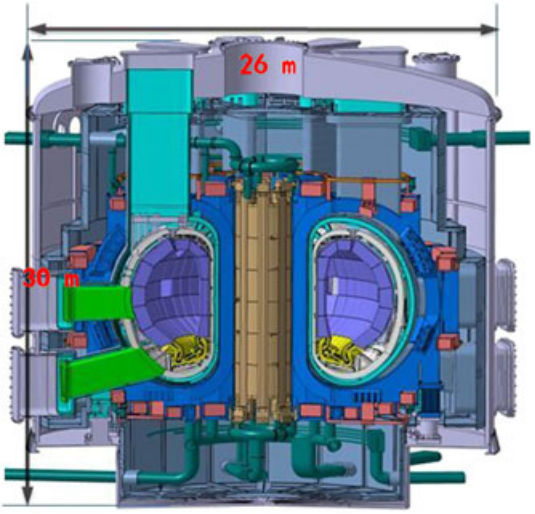

Figure 1. Overview of CFETR tokamak. [Colour figure can be viewed at wileyonlinelibrary.com]

CFETR design does while the HTS insert coils use Bi-2212 round wire, and conductor type of both parts is round-in-square cable in conduit conductor, as shown in Figure 3. Each LTS coil consists of six sextuple pancakes with 10×6 turns, and each HTS coil is made of seven quadruple pancakes with 5×4 turns. The selection of Bi-2212 takes advantages of its isotropic magnetic field dependency of critical current density and the convenience of fabricating into a cable in conduit conductor configuration compared with REBCO tape. Although silver content of Bi-2212 wire could be highly activated by neutron irradiation [8], the shield effect provided by blanket as well as toroidal field magnet and the outer LTS part could release this problem. Table I shows the up-to-date version of the geometric and operating parameters of the two conductors.

This paper mainly focuses on the stability analysis of the HTS conductor because the outer Nb3Sn conductor is almost the same as the former design and has been studied a lot. The calculation using code THEA (thermal hydraulic and electric analysis of superconducting cable) concentrates on one quadruple pancake, a cable with total length of 150 m. The stability study includes three parts. At the first step, the influence of AC loss on stability of Bi-2212 conductor during current ramp-up is discussed. The next part focuses on the effect of different kinds of perturbations with variable duration and length on stability margin. At last, the influence of inlet pressure and pressure drop of helium on stability margin is studied.

2. A SIMPLIFIED 1-D MODEL

In the simulation, a simplified 1-D model of the superconducting cable is established. This model includes a steel outer shell, helium in both bundle region and central hole, and cable strands consisting of superconductor

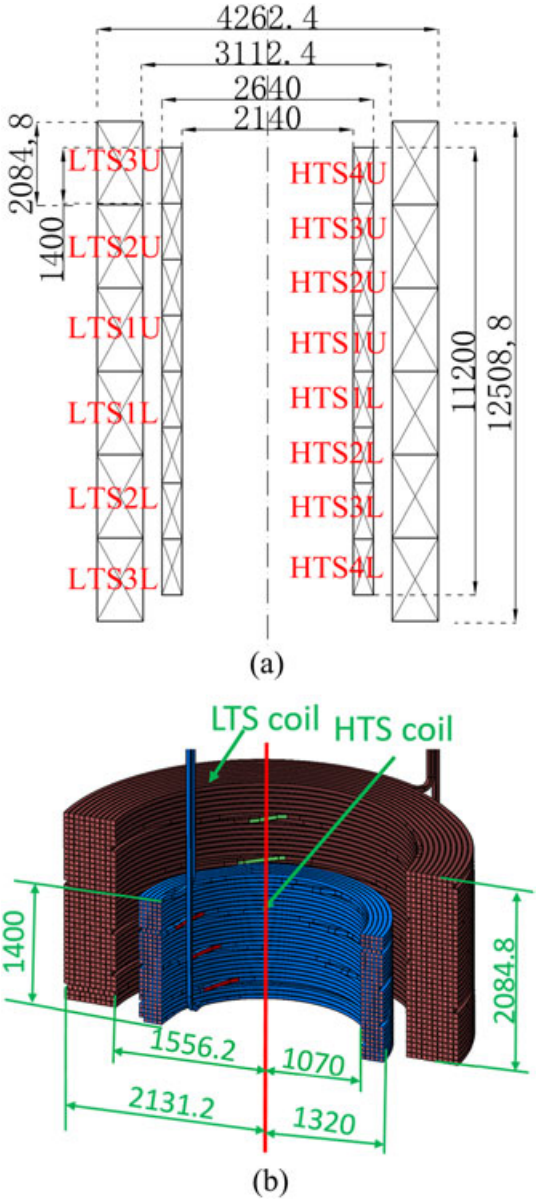

Figure 2. Geometry of the hybrid magnet (a) and the two kinds of windings (b) (unit: mm). [Colour figure can be viewed at wileyonlinelibrary.com]

strands and copper stabilizers. The strands are considered only contact with bundle helium. Another important presumption is that all the components of the cable have homogenized characteristics in cross-section. This kind of presumption is taken because of the tremendous difference between longitudinal and transverse dimension, 150 m and 46 mm, respectively, in this case.

With aforementioned assumptions, the THEA code deals with stability analysis by solving and coupling a series of partial differential equations about thermal, hydraulic, and current distribution problems; all of which

Int. J. Energy Res. 2017; **41**:1277–1286 © 2017 John Wiley & Sons, Ltd.
DOI: 10.1002/er

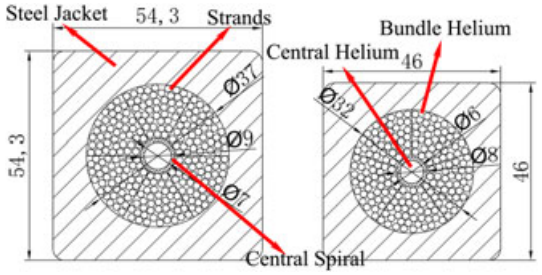

Figure 3. Cross-section of low-temperature superconductors (left) and high-temperature superconductors (right) cable in conduit conductor (unit: mm). [Colour figure can be viewed at wileyonlinelibrary.com]

can be written as a general form of a parabolic-hyperbolic system as follows [9,10],

$$\boldsymbol{m}\frac{\partial \boldsymbol{u}}{\partial t}+\boldsymbol{a}\frac{\partial \boldsymbol{u}}{\partial x}-\frac{\partial}{\partial}\left(\boldsymbol{d}\frac{\partial \boldsymbol{u}}{\partial x}\right)-\boldsymbol{s}\boldsymbol{u}=\boldsymbol{q} \tag{1}$$

where the matrices m, a, d, s, and the vector q vary in different problems. The details of the partial differential equations and the handling of their coupling can be found in reference [9,10], which are not intended to be shown here given space limitation.

As is known to all, the current carrying capacity of superconductor, namely, critical current density, deeply depends on the magnetic field and temperature of the conductors while the critical magnetic field is also related to temperature. For a certain superconductor, the relations mentioned earlier can be summarized as a scaling law. The scaling law for Bi-2212 conductor is as follows [11,12]:

$$\begin{aligned} B_c &= B_{c0}\cdot e^{-\alpha t} \\ T_c &= \frac{T_{c0}}{\alpha}\cdot\ln\left(\frac{B_{c0}}{B}\right) \\ J_c &= C_0\cdot\left[(1-\chi)\cdot(1-t)^{\gamma}\cdot\frac{B_0}{B+B_0}+\chi\cdot(1-t)^{\gamma}\cdot e^{-\beta b}\right] \end{aligned} \tag{2}$$

where B_c, T_c, and J_c are respectively irreversibility magnetic field, temperature, and current density while $t = T/T_{c0}$ is normalized temperature and $b = B/B_{c0}$ is normalized magnetic field. B_{c0} is the maximum irreversibility field at zero temperature, which is 465.5 T. T_{c0} is the maximum critical temperature at zero field, which is 87.1 K. The characteristic field B_0 has a small value of 0.075 T. Other fitting constants are $\alpha = 10.33$, $\beta = 6.76$, $\gamma = 1.73$, $\chi = 0.55$. On the other hand, for a giving operating current density, there also exists a temperature limit above which superconductor begins to share current with stabilizer until temperature reach T_c. This current sharing temperature (T_{cs}) is obtained by iteratively solve the aforementioned equations.

Main input parameters used in THEA corresponding to the geometry and operating condition of cable used in simulation are shown in Table II. The maximum magnetic field and current is considered, to ensure a conservative result.

The n-power and E_0 are two parameters used to describe the electric field versus current characteristic of a superconductor by the following relationship [13],

$$E_s = E_0\left(\frac{J_s}{J_c}\right)^n \tag{3}$$

Table I. Geometric and operating parameters of the two coils.

Parameters	LTS outer coil	HTS inner coil[a]
SC strand type	Nb3Sn	Bi2212
Maximum operating current	55.56 kA	50 kA
Maximum operating magnetic field	10.1 T	16.79 T
Operating temperature	4.2 K	4.2 K
Void fraction	30%	30.4%
Cable length	700 m	150 m
Coil configuration	Sextuple pancake	Quadruple pancake
Turns of each pancake	10 × 6	5 × 4
Cable diameter	37	32
316LN circle in square jacket	54.3 × 54.3 mm^2	46 × 46 mm^2
Outer/Inner diameter of central spiral	9 mm/7 mm	8 mm/6 mm
SC strand diameter	0.83 mm	0.8 mm
Cable configuration	(2sc + 1) × 3 × 4 × 6 × 6	(1sc + 1) × 3 × 5 × 7 × 5
SC strands numbers	864	525
Cu: non-Cu in cable	2	1
RRR	100	100

SC, superconducting; RRR, Residual-resistance ratio; LTS, low-temperature superconductors; HTS, high-temperature superconductors.

Table II. Input parameters in simulation with THEA code.

Input parameters	Value
Length (m)	150.0
Current (A)	50,000
Magnetic field (T)	16.79
Area of copper (mm^2)	262.5
Area of superconductor (mm^2)	262.5
Area of shell (mm^2)	1311.78
Area of bundle helium (mm^2)	229
Area of central helium (mm^2)	50.24
Hydrodynamic diameter of bundle helium (mm)	0.46
Hydrodynamic diameter of central spiral (mm)	8
Perimeter of bundle helium (mm)	1866
Perimeter of shell (mm)	100.5
Perimeter of central spiral (mm)	25.13
Perforation of central spiral	27.2%
n-Power	10
E0 (V/m)	1.0×10^{-4}
Helium inlet pressure (MPa)	0.60
Helium pressure drop (MPa)	0.12

where E_s and J_s are, respectively, the superconductor electric field and current density. The n-power is estimated based on the experiment data at 15 T, and a general value for E_0 is chosen [14].

3. AC LOSS AND STABILITY DURING CURRENT RAMP

AC loss is one of the most important facts that could disturb the normal operation of the superconducting cable. Here we discuss the hysteresis loss produced during current ramp of the coils, and the current in a cable is regarded linearly increases to the maximum. Because this paper mainly deals with the insert HTS coils, we assume the outer LTS coils operate with a constant current to generate background magnetic field at the HTS region; the maximum of which is about 10 T. For HTS insert coils, we consider four different current ramp rates to calculate AC loss and then discuss the stability.

In calculating AC loss, a simplified symmetry model of the hybrid magnet is built by finite element method, as shown in Figure 4. The outer LTS coils (red color) are treated as normal conductor with constant resistivity and are given constant current to provide background magnetic field for HTS coils. The inner HTS coils are divided into two types. Except the small square areas (blue color) are treated as superconductor by applying E–J characteristic mentioned earlier, the rest parts (yellow color) are also regarded as normal conductor to reduce computational complexity. The current in HTS parts grows linearly from zero to the max value with in 33.6, 16.8, 11.2, and 8.4 s in the four cases. All the coils are surrounded by air (gray color). Then, the evolution of the magnet system is simulated by solving following equations [15],

$$\begin{aligned} \nabla\times\boldsymbol{E} &= -\mu_0\mu_r\frac{\partial \boldsymbol{H}}{\partial t} \\ \nabla\times\boldsymbol{H} &= \boldsymbol{J} \end{aligned} \tag{4}$$

The instantaneous hysteresis loss per length is calculated by integration as follows,

$$P_h = \int_s E_\varphi \cdot J_\varphi ds \tag{5}$$

The integration is carried among the 100 superconducting areas. Then, the instantaneous and integrated loss per length among a cable is estimated by multiplying by 25, as shown in Figure 5. The relation between instantaneous loss and time can be fitted as follows:

$$loss(t) = A_2 + \frac{(A_1 - A_2)}{1 + \left(\frac{t}{t_0}\right)^p} \tag{6}$$

A_1, A_2, t_0, and p vary in the four cases, as shown in Table III. Although this kind of model does not fully match

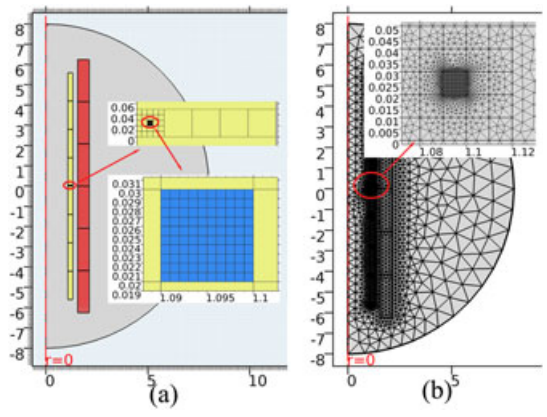

Figure 4. The finite element method model for calculation of AC loss, including both high-temperature superconductors and low-temperature superconductors coils and air (unit: m). [Colour figure can be viewed at wileyonlinelibrary.com]

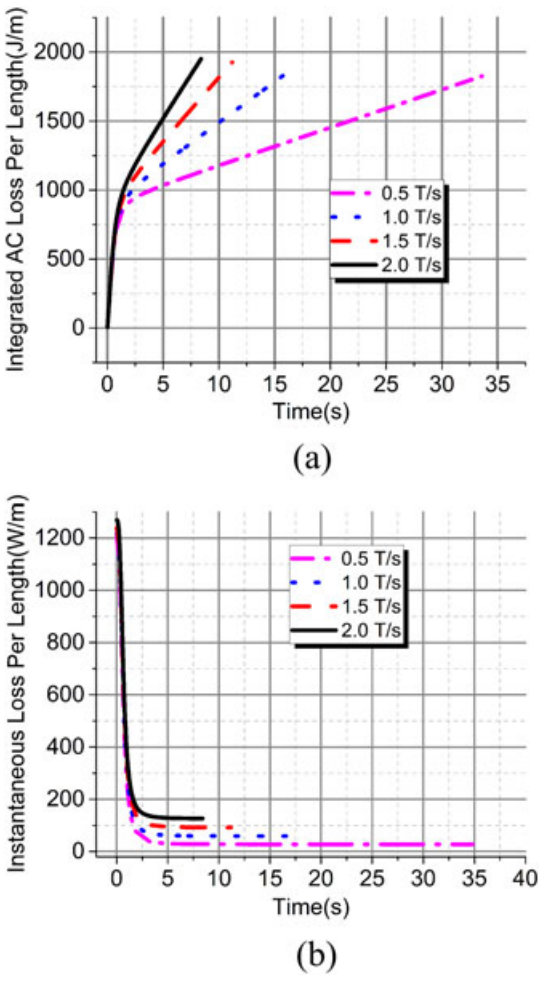

Figure 5. The integrated (a) and instantaneous (b) AC loss among a cable for four cases with different ramp rates. [Colour figure can be viewed at wileyonlinelibrary.com]

Int. J. Energy Res. 2017; **41**:1277–1286 © 2017 John Wiley & Sons, Ltd.
DOI: 10.1002/er

Table III. Fitting parameters of instantaneous loss.

	A_1(W)	A_2(W)	t_0(s)	p
0.5 T/s	1203	27.39	0.628	2.8488
1.0 T/s	1217	58.91	0.638	2.8779
1.5 T/s	1238	91.85	0.645	2.9023
2.0 T/s	1268	125.51	0.648	2.9117

the real magnet, difference of the four cases is still well described.

Figure 6 shows the temperature distribution of strands in longitudinal direction at different times. We can see that for ramp rate of 0.5, 1.0, and 1.5 T/s, the temperature of cable strands begins to decrease when current reach the maximum after which the AC loss is unloaded. This means the AC loss during current ramp does not make the superconducting system quench. However, in the case of 2.0 T/s, the temperature of strands continues to increase after the AC loss ends. Considering the total loss energy is almost the same for the four cases, the final quench indicates that heat is deposited into the system too quick, and temperature of some area exceeds the T_{cs}. After external heat is canceled, the joule heat generated by the normal zones exceeds the cooling capacity of the cable and leads to the final quench. Figure 7 shows the evolution of normal zone length of superconductor in the four cases, from which we can get same conclusion as mentioned earlier.

4. PERTURBATIONS WITH VARIED DURATIONS AND LENGTHS

4.1. Spectrum of stability margin

Besides AC loss, there are many other kinds of perturbations that may happen during operation of a superconducting magnet, like flux jump, nuclear heat, and wire motion. The duration and length of these perturbations range widely, which may have different effect on the stability of the cable. In the light of that, stability

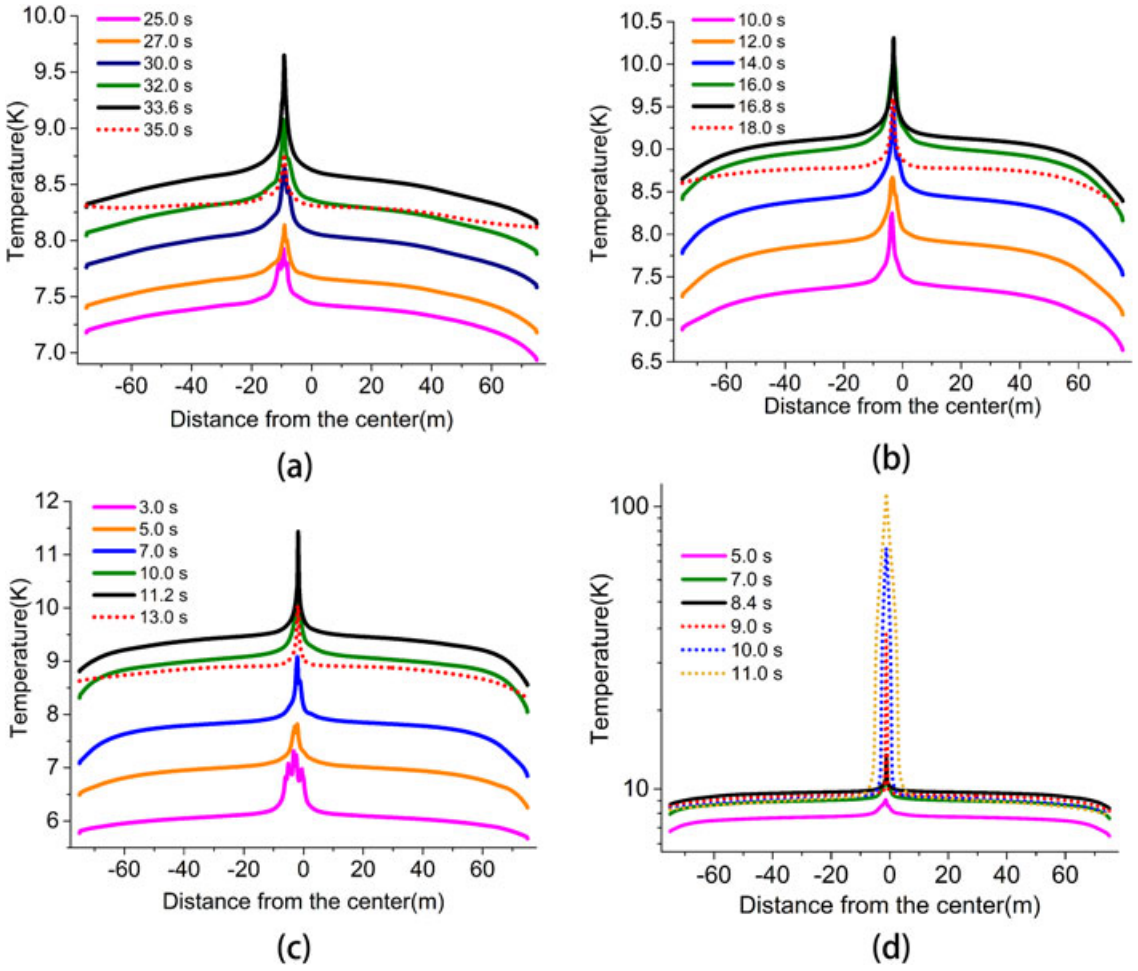

Figure 6. Temperature distribution of strands with different ramp rates; (a) 0.5 T/s, (b) 1.0 T/s, (c) 1.5 T/s, and (d) 2.0 T/s. [Colour figure can be viewed at wileyonlinelibrary.com]

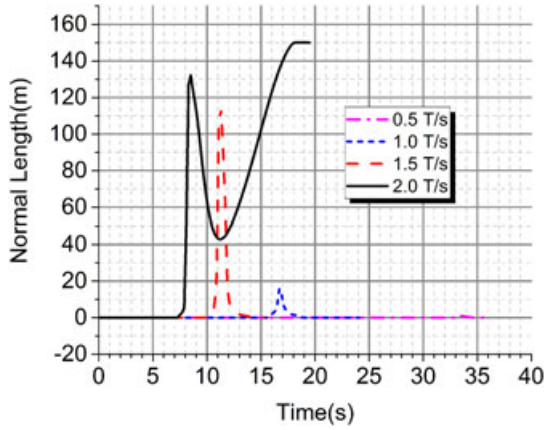

Figure 7. Evolution of normal-zone length of superconductor in the four cases. [Colour figure can be viewed at wileyonlinelibrary.com]

margins of different perturbations with variable durations (0.001–1 s) and lengths (0.01–10 m) are calculated to figure out the potential regularity and provide reference for pertinent optimization of the conductor.

Stability margin also called energy margin defined by Eq. (7) is calculated using a trial-and-error procedure [13], to ascertain how much heat can be deposited into superconducting cable without thermal runaway,

$$E = \frac{Q_0 \cdot L \cdot T}{(A_{sc} + A_{Cu}) \cdot L} \tag{7}$$

As Eq. (7) shows, besides the maximum power density per length (Q_0, unit: W/m), stability margin is also related to duration (T, unit: s) of the disturbance as well as the total area of conductors, which means the area of strands including both superconductors (A_{sc}, unit: m^2) and copper stabilizers (A_{Cu}, unit: m^2). And because the length (L, unit: m) can be canceled, stability margin is free from it.

Figure 8 shows stability margin as a function of duration for four different lengths. As we can see, the system shows sufficient stability against disturbance. Even for the most stringent situation, the stability margin still exceeds 100 mJ/cc (1 mJ/cc = 1000 J/m^3), indicating the current cable design has good stability.

Before about 0.01 s, stability margin increases with duration almost linearly regardless of perturbation length.

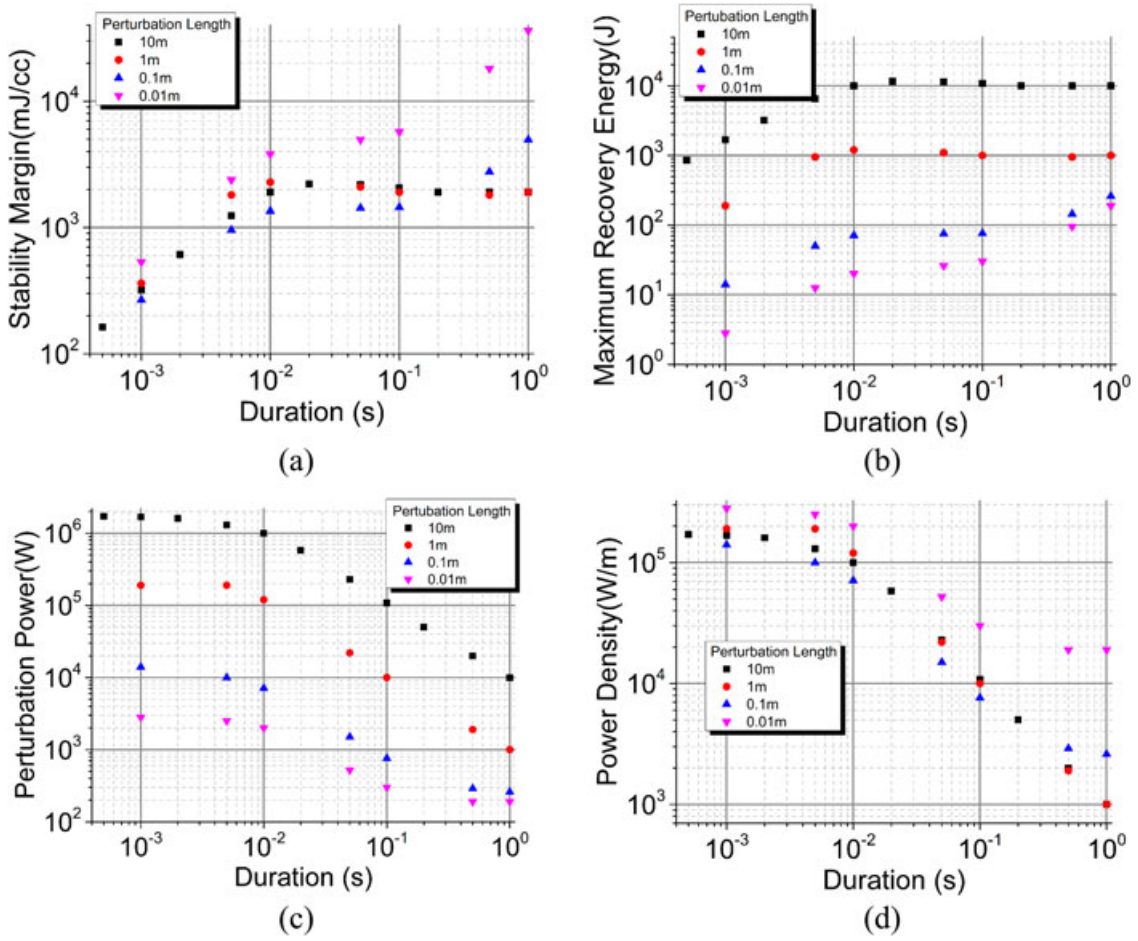

Figure 8. Stability margin (a), maximum recovery energy (b), perturbation power (c), and perturbation power density (d) as functions of duration for different perturbation lengths. [Colour figure can be viewed at wileyonlinelibrary.com]

Int. J. Energy Res. 2017; **41**:1277–1286 © 2017 John Wiley & Sons, Ltd.
DOI: 10.1002/er

After that, there comes divergence: for perturbation with length of 1 and 10 m (called long perturbation below), stability margin varies slowly and gradually becomes constant. However, things are quite different in the case of 0.1 and 0.01 m (called short perturbation below), in which stability margin shows a plateau region between 0.01 and 0.1 s and then continues increasing. The shorter is the length, the shorter is the plateau region and the greater is the increment. Similar result was observed in LTS conductor [16]. To investigate the reason for this kind of difference, here, we also show the variation curve of maximum recovery energy (MRE), heating power of the perturbation, and the corresponding power density in Figure 8. The relationships among them are as follows:

$$\begin{aligned} E &= \frac{E_0}{(A_{sc}+A_{cu})\cdot L} \\ {}_{E0} &= P\cdot T \\ P &= Q_0\cdot L \end{aligned} \tag{8}$$

where E is the stability margin mentioned earlier, P is power of perturbation and Q_0 is the power density per length. E_0 is MRE, a threshold that if the perturbation energy is below, the magnet system can 'recovery' to the superconducting state after the perturbation is loaded. A similar definition, minimum runaway energy is also used [17,18]. From Figure 6, we can see that the MRE has the same trend with the stability margin against duration. This is understandable because the only discrepancy between these two quantities is a constant factor related to perturbation length, which also causes the difference in MRE. Figure 6 also indicates that although stability margin of long length, that is, 10 and 1 m is lower, the MRE of which is actually higher than short perturbations.

Similarly, the heating power and power density that also differ by a length related factor have the same trend: The perturbation power and power density hardly change with duration until it increases to some degree. After that, both of them began to decrease linearly and then branch when duration is up to about 0.1 s: The curve keeps the downside for long perturbations but settles down for short perturbation, and the shorter is the length, the earlier it enters stable state, and the higher is the power density.

Two important conclusions can be refined from the aforementioned discussion: In the sight of energy including MRE and stability margin, perturbation with longer length tends to be stable as duration increases, while in terms of power, perturbation with shorter length is going to stabilize as duration increases.

4.2. A qualitative explanation

Figure 9 shows the variation of temperature distribution of strands for perturbations with typically long and short length, 10 and 0.1 m, respectively, in the case of quench triggered by minimum quench energy. For long

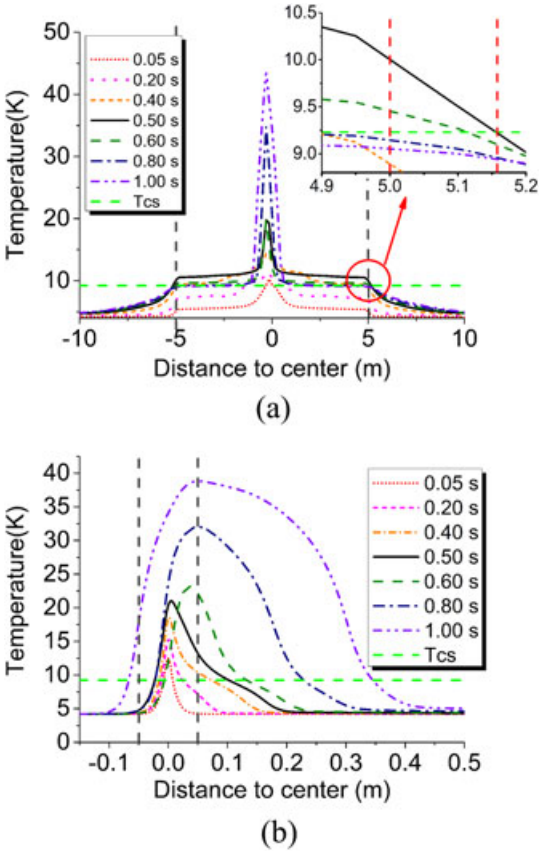

Figure 9. Temperature distribution of strands for two typical perturbations; (a) perturbation with length of 10 m, (b) perturbation with length of 0.1 m; duration for both perturbations is 0.5 s. [Colour figure can be viewed at wileyonlinelibrary.com]

perturbation, the temperature distribution can be described as two symmetrical stairs with a sharp peak in the middle. The first stair divided by the vertical dash line is about 10 m, exactly the same with the perturbation length. On the first stair, neglecting the central peak, the other region is almost flat. Beyond the vertical dash line, the temperature gradually goes down to another flat region, namely, the second stair.

However, the temperature distribution of short perturbation only shows symmetry in a small period. With time increase, temperature begins to propagate along the downstream direction of helium, which is supposed to be attributed to the effect of helium [19]. And there is only one stair with a peak getting fatter and propagating. It should also be noted that the propagation of temperature along longitudinal direction is appreciable only when time is sufficiently long (more than 0.2 s in Figure 9).

Moreover, the propagation of normal zone, namely, the region where temperature is higher than current sharing temperature, which is about 9.2 K with a high-temperature margin of 5 K here, also shows difference in the two cases. For long perturbation, it can be seen that the growth of normal zone length, which is only several decimeters, is trivial

compared with the perturbation length. Whereas for short length perturbation, the normal zone length grows remarkably and reaches about four times of the perturbation length at the time of 1 s. Indeed, the grown normal zone lengths in two cases are similar in quantity, but things become quite different when comparing with the original perturbation length.

Figure 10 also gives a comparison of temperature distribution between strands and bundle helium, from which we can see that for long perturbation, temperature of strands and bundle helium is very close except for the narrow peak region. On the other hand, for short perturbation, temperature of strands is much higher than temperature of helium.

Given all this, we can see that for long perturbation, the effect of heat conduction of both strands and helium is rather limited compared with the convection heat transfer with helium. This limitation of heat conduction also leads to heat accumulation in perturbation center. When the duration reaches some threshold, there is sufficient time for strands to exchange heat with helium, leading to stability margin mainly restricted by the specific heat capacity of strands and helium, which is the reason why long-length perturbation shows a limitation in energy.

For short-length perturbation, when duration is short, convection heat transfer also plays a dominant role on cooling strands, which result in the similar trend of stability margin with long perturbation. However, with duration increase, the effect of longitudinal heat conduction is becoming more and more important; making the system can tolerate more perturbation energy. And the shorter is the length, the effect of longitudinal heat conduction shows earlier.

There are two more anomalies that need to be explained, the sharp peak in the temperature distribution in the long-perturbation case as well as the AC loss case and the asymmetry of temperature distribution in the short-perturbation case. Considering all the concerning conditions, a reasonable inference is the effect of helium. Figure 11 shows the temperature distribution of strands in both two cases without helium cooling. Besides the remarkable increase of temperature and normal zone

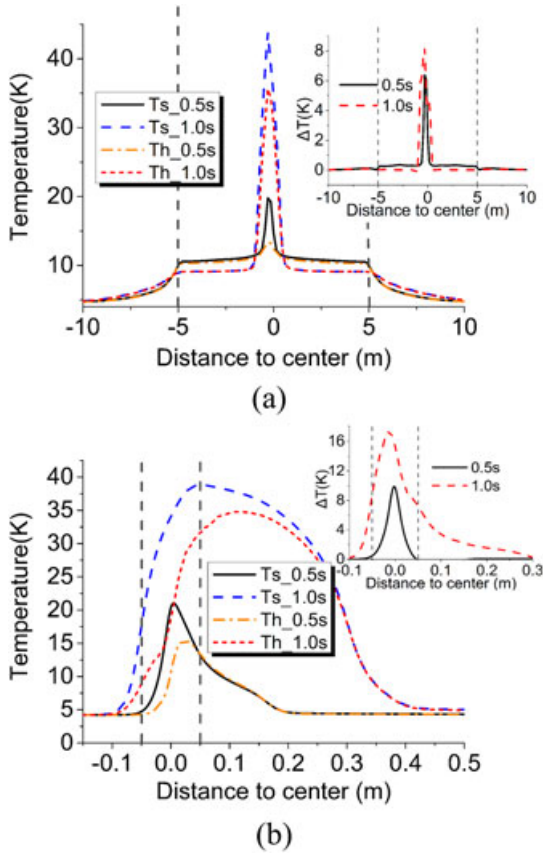

Figure 10. Comparison of temperature distribution between strands (Ts) and bundle helium (Th) as well as their temperature difference (shown at top-right in each picture) at the time of 0.5 and 1.0 s; (a) perturbation with length of 10 m, (b) perturbation with length of 0.1 m; duration for both perturbations is 0.5 s. [Colour figure can be viewed at wileyonlinelibrary.com]

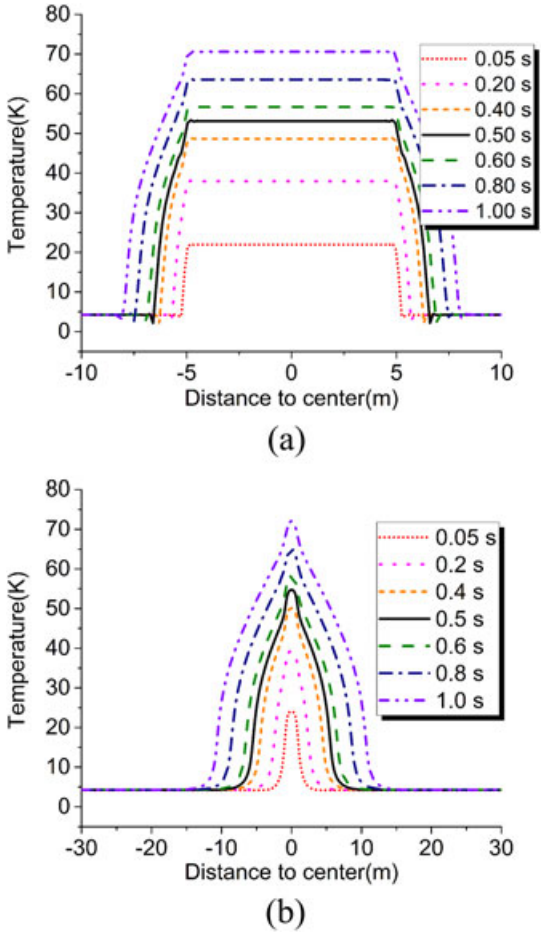

Figure 11. Temperature distribution of strands without helium cooling; (a) perturbation with length of 10 m, (b) perturbation with length of 0.1 m; duration for both perturbations is 0.5 s. [Colour figure can be viewed at wileyonlinelibrary.com]

Int. J. Energy Res. 2017; **41**:1277–1286 © 2017 John Wiley & Sons, Ltd.
DOI: 10.1002/er

length, we can see that the temperature distributions in both cases are symmetrical. The plateau in long-perturbation case and the sharp peak in short-perturbation case are related to the different effect of heat conduction, as discussed earlier. Now we make some inferences about the two anomalies. When helium is heated by strands, its flow condition may change a lot affecting both heat transfer and heat removal capability, which in turn influence the temperature of strands. Together with the difference in heat conduction, make the temperature distribution in the two cases shows significant difference. The coupling effect between strands and helium inevitable needs further study, which is beyond our qualitative explanation.

5. PRESSURE AND PRESSURE DROP OF HELIUM

The convection heat transfer between strands and helium, deeply dependent on the flowing state of helium, plays a major role in the cooling of cable. Here we consider two crucial parameters that are relevant to helium state: inlet pressure and pressure drop (substituted with pressure drop per unit below). The inlet pressure varies from 0.5 to 1.2 MPa, and the pressure drop varies from 0.0002 to 0.0014 MPa/m that is 0.03 to 0.2 MPa for the total length. Two kinds of perturbation are chosen as comparison: one with length of 10 m and duration of 0.2 s (called long perturbation below) and another with 0.01 m and 0.001 s (called short perturbation below).

Figure 12 shows the stability margin of the two perturbations as a function of pressure drop in different inlet pressure. It can be seen clearly that although the variation of stability margin of the two perturbations shows similar trend, the range of variation is quite different. For long perturbation, the variation of stability margin between pressure drops of 0.0002–0.0014 MPa/m is about 200 mJ/cc, while in the case of short perturbation is about 2500 mJ/cc.

This difference in magnitude can also be qualitatively explained from the temperature distribution. As it is discussed earlier, the restriction for the stability margin of long perturbation is mainly the specific heat capacity of strands and bundle helium especially when duration is long enough. Therefore, even the convection heat transfer between strands and bundle helium is enhanced by raising the pressure drop of helium, the improvement to stability margin is still limited. In the case of short perturbation, however, on the one hand, the significant longitudinal heat conduction employs more strands to deposit the perturbation, while on the other hand, the strands and bundle helium still have some differences in temperature because of the short duration. These conditions leave spaces for the improvement of stability by enhancing the pressure drop.

When it comes to pressure, things get a little complicated. Although in most cases, stability margin increases with inlet pressure, there exist some exceptions in which

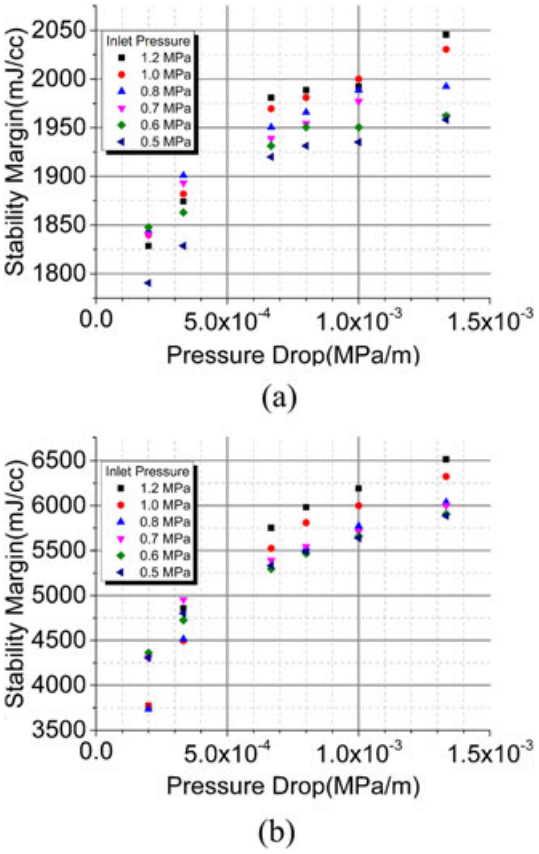

Figure 12. Stability margin of the two perturbations as a function of pressure drop in different inlet pressure; (a) perturbation with length of 10 m and duration of 0.2 s, (b) with length of 0.01 m and duration of 0.001 s. [Colour figure can be viewed at wileyonlinelibrary.com]

stability margin begins to go down when inlet pressure reaches some degree especially when pressure drop is low. A rational supposition for this is that in these situations, the properties changing of helium like density and specific heat capacity driven by pressure lead to a worse heat exchange ability. A detail study about this may be carried out in the future.

6. CONCLUSIONS

Stability analysis of the Bi-2212 cable of a hybrid magnet has been carried out based on a 1-D simplified model.

The effect of AC loss during current ramp-up is simplified as a perturbation along the overall cable. Simulation shows for ramp rate of 0.5, 1.0, and 1.5 T/s that the cable will operate steadily, while for a higher rate of 2.0 T/s, it will quench.

Stability margins under perturbations with different durations and lengths are also calculated. The high margin indicates that the present cable design has good stability. The result also shows that for different perturbation

lengths, trends of stability margin diverge when duration increases to about 0.01 s: for perturbations with longer lengths (10 and 1 m), stability margin increases slowly and finally becomes constant, whereas for those with shorter lengths (0.1 and 0.01 m), stability margin continues its upward tendency. The difference is believed to be caused by the different effects of heat conduction in different situations.

At last, the effect of inlet pressure and pressure drop of helium on stability margin is discussed for two typical perturbations. The results show these two factors have much higher influence on short perturbation than long perturbation, which is also related to the heat conduction feature of different perturbations and supports our former conclusion.

ACKNOWLEDGEMENTS

The author would like to express his appreciation to all the members of CFETR design team. This work was supported in part by the National Natural Science Foundation of China under Grant No.51507173, Anhui Province Natural Science Foundation of China under Grant No.1608085QE93, and Youth Innovation Promotion Association of Chinese Academy of Sciences under Grant No.2015266.

REFERENCES

1. Song YT, Wu ST, Li JG, *et al.* Concept design of CFETR tokamak machine. *IEEE Transactions on Plasma Science* 2014; **42**:503–509.
2. He X, Zheng JX, Zhang H, Liu XF. Stability analysis of the conductors for CFETR poloidal field coils. *Fusion Engineering and Design* 2015; **95**:13–19.
3. Liu XF, Zheng JX, Luo ZP et al. Conceptual design and analysis of CFETR magnets. Symposium On Fusion Engineering (SOFE), *2013 IEEE 25th Symposium on San Francisco*, CA, 2013.
4. Schultz JH, Antaya T, Feng J et al., "The ITER Central Solenoid," 21st IEEE/NPSS Symposium on Fusion Engineering - SOFE 05, pp. 142-145, 2006.
5. Uglietti D, Bykovsky N, Wesche R, Bruzzone P. Development of HTS conductors for fusion magnets. *IEEE Transactions on Applied Superconductivity* 2015; **25**:1–6.
6. Weijers HW, Trociewitz UP, Markiewicz WD, *et al.* High field magnets with HTS conductors. *IEEE Transactions on Applied Superconductivity* 2010; **20**:576–582.
7. Zheng JX, Song YT, Liu XF et al. Concept design of hybrid superconducting magnet for CFETR Tokamak reactor. Symposium On Fusion Engineering (SOFE), 2013 IEEE 25th Symposium on San Francisco, CA, 2013.
8. Yanagi N, Ito S, Terazaki Y, *et al.* Design and development of high-temperature superconducting magnet system with joint-winding for the helical fusion reactor. *Nuclear Fusion* 2015; **55**.
9. Bottura L. Modelling stability in superconducting cables. *Physica C* 1998; **310**:316–326.
10. Bottura L, Rosso C, Breschi M. A general model for thermal, hydraulic and electric analysis of superconducting cables. *Cryogenics* 2000; **40**:617–626.
11. Laan DC, Eck HJN, Haken B, Schwartz J, Kate HHJ. Temperature and magnetic field dependence of the critical current of BSCCO tape conductors. *IEEE Transactions on Applied Superconductivity* 2001; **11** (1):3345–3348.
12. Wesche R. Temperature dependence of critical currents in superconducting Bi-2212/Ag wires. *Physica C* 1995; **246**:186–194.
13. Iwasa Y. *Case Study in Superconducting Magnets*. Springer US, 2009.
14. Lombardo V, Barzi E, Turrioni D, Zlobin AV. Critical currents of YBa2Cu3O7-delta tapes and Bi2Sr2CaCu2Ox wires at different temperatures and magnetic fields. *IEEE Transactions on Applied Superconductivity* 2011; **21**:3247–3250.
15. Wang L, Zheng JX, Jiang F, Kang R. Numerical simulation of AC loss in 2G high-temperature superconducting coils with 2D-axisymmetric finite element model by magnetic field formulation module. *Journal of Superconductivity and Novel Magnetism* 2016; **29**:2011–2018.
16. Bottura L, Calvi M, Siemko A. Stability analysis of the LHC cables. *Cryogenics* 2006; **46**:481–493.
17. Richard LS, Bessette D, Zanino R. Stability analysis of the ITER PF coils. *IEEE Transactions on Applied Superconductivity* 2009; **19**:1496–1499.
18. Hahn S, Song J, Kim Y, *et al.* Design study on a 100-kA/20-K HTS cable for fusion magnets,". *IEEE Transactions on Applied Superconductivity* 2015; **25**:1–5.
19. Marinucci C, Bottura L, Calvi M, Wesche R. Quench analysis of a high-current forced-flow HTS conductor model for fusion magnets. *IEEE Transactions on Applied Superconductivity* 2011; **21**:2445–2448.